Paleoceanography and Paleoclimatology

Supporting Information for

Seawater lead isotopes record early Miocene to modern circulation dynamics in the Pacific sector of the Southern Ocean

Huang Huang[1,2,3,4]*, Marcus Gutjahr[1], Zhaoyang Song[3,5], Jan Fietzke[1], Martin Frank[1], Gerhard Kuhn[6], Claus Dieter Hillenbrand[7], Marcus Christl[8], Dieter Garbe-Schönberg[9,10], Tyler Goepfert[11], Anton Eisenhauer[1]

[1] GEOMAR Helmholtz Centre for Ocean Research Kiel, Wischhofstraße 1-3, 24148 Kiel, Germany

[2] School of Marine Sciences, Sun Yat-Sen University, Zhuhai, Guangdong 519082, China

[3] Southern Marine Science and Engineering Guangdong Laboratory (Zhuhai), Zhuhai, Guangdong 519082, China

[4] Laboratory for Marine Geology, Qingdao National Laboratory for Marine Science and Technology, Qingdao 266071, China

[5] School of Atmospheric Sciences, Sun Yat-Sen University, Zhuhai, Guangdong 519082, China

[6] Alfred-Wegener-Institut Helmholtz-Zentrum für Polar- und Meeresforschung, Am Alten Hafen 26, 27568 Bremerhaven, Germany

[7] British Antarctic Survey, High Cross, Madingley Road, Cambridge CB3 0ET, UK

[8] ETH Zurich, Laboratory of Ion Beam Physics, Otto Stern Weg 5, CH-8093 Zurich, Switzerland

[9] Institute for Geosciences, Christian-Albrechts-University, Ludewig-Meyn-Straße 10, 24118 Kiel, Germany

[10] Department of Physics and Earth Sciences, Jacobs University Bremen gGmbH, 28759 Bremen, Germany

[11] School of Earth and Space Exploration, Arizona State University, Tempe, AZ 85287, USA

Contents of this file

Introduction

The Supporting Information here include dating methods which are used to build the age model of crust Haxby, and the laser ablation and conventional methods that are used to extract the seawater Pb isotope records.

Methods:

^{10}Be/^{9}Be and high-resolution cobalt (Co) flux methods. For the last 11.75 Ma, the average crust growth rates and age–depth relationships were determined directly from the ^{10}Be/^{9}Be profile. Due to the ^{10}Be half-life of 1.387 Myr (Chmeleff et al., 2010), ^{10}Be concentrations at ages older than 11.75 Ma are not detectable any more (>8 half-lives), and the ages older than 11.75 Ma had to be estimated based on a Co-constant flux model (Manheim, 1986; Frank et al., 1999).

The samples for ^{10}Be and ^{9}Be analysis were manually drilled from 10 different depths in the Fe-Mn crust section (Figure S1). The samples were then dissolved in 6 M HCl and split into two aliquots for separate ^{10}Be and ^{9}Be measurements. The ^{9}Be concentration was determined using the AGILENT 7900 ICP-MS at the Institute of Geosciences, Kiel University, Germany, following standard procedures (Garbe-Schönberg, 1993). The 1σ uncertainty of the ^{9}Be measurements is 5%. The ^{10}Be concentration in the second aliquot was measured using an isotope dilution method. After adding a known amount of ^{9}Be carrier in the weighed sample aliquot, the sample solution was purified for Accelerator Mass Spectrometry (AMS) analysis according to an established method (Henken-Mellies et al., 1990; Frank et al., 1994). The ^{10}Be concentrations were measured at the AMS Tandy facility at ETH Zürich, Switzerland. The repeatedly measured ^{10}Be/^{9}Be ratios of samples and standards were normalized relative to the internal ^{10}Be standards S2007N and S2010N with nominal values of ^{10}Be/^{9}Be = 28.1 x10^{-12} and ^{10}Be/^{9}Be = 3.3 x 10^{-12}, respectively (Christl et al., 2013). S2007N and S2010N have been calibrated relative to the primary standard ICN 01-5-1 with a nominal ^{10}Be/^{9}Be ratio of 2.709 x 10^{-11} (Nishiizumi et al., 2007). The uncertainties of the ^{10}Be measurements are presented in the Table S1.

The concentrations and intensities of Fe, Mn and Co in the sample slide were measured by electron microprobe (EMP) after laser ablation analysis. Instrumental conditions for electron microprobe analysis are shown in Table S2. The measurements were carried out at GEOMAR Kiel, Germany, using a JEOL JXA 8200 "Superprobe". WDS (wavelength dispersive X-ray spectroscopy) elemental maps were acquired with 30 µm resolution for the whole sample in three steps under the same conditions. Five standards (PbS, Fe_2O_3, VG-2, KAN1, Rhodonite) were analysed using exactly the same instrumental conditions as 5x5 pixel WDS maps. From these standard measurements the intensity-concentration

conversion was calculated as shown in the Table S3. The Fe and Mn compositions in this crust show typical hydrogenous growth (Figure. S2).

The Co-flux data was calculated using the following equation modified from previous studies (Manheim, 1986; Frank et al., 1999):

$$\textbf{Growth rate}\ (\textbf{mm/Ma}) = \frac{\mathbf{0.31}}{(\mathbf{Co_{Intensity}/142})^{\mathbf{2.5}}}$$

$Co_{intensity}$ is the average measured Co signal intensity of ten data points which are in parallel with the laser track (Figure S1 and S2).

Pb isotope compositions analysed by LA-MC-ICP-MS. Prior to laser ablation measurements, the sample surface was pre-ablated by triple laser pulses with 3 J cm^{-2} laser power density in order to eliminate potential surface contamination. Two different laser ablation operation settings were applied for different timescale resolution analysis (Table S7). Each analysis consisted of a 30-second gas blank and 60-second sample acquisition signal and all signals were collected for static isotopic composition analysis. The instrumental mass fractionation was corrected using the linear regression normalization method (Fietzke et al., 2008) bracketing samples with NIST SRM 610, USGS NOD-A-1 and USGS NOD-P-1 standards. The USGS NOD-A-1 and NOD-P-1 standards are original ferromanganese nodule powders that were directly pressed into pellets without chemical binder for LA work.

During the LA experiments, we found that the ^{204}Hg interference and Pb isotope signal intensities were the two most critical factors which affected the data quality, so the standards were analysed with different LA unit settings (Table S8) to match the Pb isotope signal intensity of the sample. The NIST SRM 610, USGS NOD-A-1 and USGS NOD-P-1 standards were chosen for mass fractionation normalization because they cover a wide $^{206}Pb/^{204}Pb$ range from 17.052 to 18.964 with different matrix compositions. For instance, NIST SRM 610 glass not only showed similarly low ^{204}Hg interference contributions as in sample crust material, but also provided comparable Pb isotope signal intensities under the applied LA condition. The USGS NOD-A-1 and NOD-P-1 pellets have a similar matrix composition as the samples. Therefore, the combination of these three different standards (NIST SRM 610, USGS NOD-A-1 and USGS NOD-P-1) provide the best evaluation towards the accuracy and precision of the measurement covering similar ^{204}Hg interference proportions, Pb isotope signal intensities and considering matrix compositions.

The foundation of our analytical strategy is based on the assumption that the Pb isotope fractionation factors between sample and the selected standards are identical when the plasma conditions of MC-ICPMS are consistent in all measurements (Fietzke and Frische, 2016). We tuned the plasma states of MC-ICPMS for sample and standard analyses to be similar with a Normalized Argon Index (NAI) value at about 1 (Fietzke and Frische, 2016). As shown in Figure S3, the calculated optimal Pb isotope fractionation factor can normalize all selected standards to their literature values, corroborating that the applied mass bias

correction is adequate. We therefore use the same calculated optimal Pb isotope fractionation factor to normalize the sample mass fractionation.

The optimal Pb isotope fractionation factor was calculated by the linear regression normalization method, modified from Fietzke et al., 2008, and achieved in two steps: (1) blank correction, (2) Hg interference correction. We here present the procedure for the normalization of $^{206}Pb/^{204}Pb$ ratio for standards as an example to describe the procedure. First, the blank correction for measured $^{206}Pb/(^{204}Pb+^{204}Hg)$ ratios was achieved by plotting the raw LA data of standards and corresponding gas blank data collected by amu 206 and amu 204. As shown in Figure S4, the amu 206 and amu 204 signals of NIST SRM 610, USGS NOD-A-1 and USGS NOD-P-1 standards show a linear relationship. After applying linear regression calculation for the data of each standard, the acquired slope value provides background (blank) corrected $^{206}Pb/(^{204}Pb+^{204}Hg)$ ratios (Fietzke et al., 2008). Secondly, we subtract ^{204}Hg interference on ^{204}Pb signal using the measured ^{202}Hg and an optimal $^{202}Hg/^{204}Hg$ ratio (R_{Hg}) instead of the literature $^{202}Hg/^{204}Hg$ value, because $^{202}Hg/^{204}Hg$ is also fractionated during the measurement and can vary between different measurement sections. The standards and sample Fe-Mn crust have variable Hg/Pb ratios (NIST SRM 610: Hg/Pb ~ 0.04%; USGS NOD-A-1: Hg/Pb ~ 0.06%; USGS NOD-P-1: Hg/Pb ~ 3.00%; PS75/247-2: Hg/Pb ~ 0.05%). The small offset between the real $^{202}Hg/^{204}Hg$ ratio and the literature $^{202}Hg/^{204}Hg$ value can have big impact on the result, especially when the Hg/Pb is high. We use the Goal Seek analysis in Excel software to determine both of the optimal R_{Hg} and optimal Pb isotope fractionation factor. A hypothesized R_{Hg}= 4 is first used to calculate preliminary $^{206}Pb/^{204}Pb$ ratios of the three standards from $^{206}Pb/(^{204}Pb+^{204}Hg)$ ratios. Literature values (NIST SRM 610: $^{206}Pb/^{204}Pb$ = 17.052; USGS NOD-A-1: $^{206}Pb/^{204}Pb$ = 18.964; USGS NOD-P-1: $^{206}Pb/^{204}Pb$ = 18.700 (Baker et al., 2004)) are divided by the preliminary $^{206}Pb/^{204}Pb$ ratios to obtain preliminary Pb isotope fractionation factors from different standards. Then, average values of all three preliminary Pb isotope fractionation factors can be calculated. Based on this average preliminary Pb isotope fractionation factor, we normalized all $^{206}Pb/^{204}Pb$ ratios for measured standards. The sum of offsets of the preliminary mass bias corrected $^{206}Pb/^{204}Pb$ ratios of these three standards from literature values is set to zero in the Goal Seek function with the R_{Hg} value as a variable. The Goal Seek analysis will give an optimal R_{Hg} value which can result in the smallest offset from the literature values. Because the optimal R_{Hg} is linked to the mass-dependent isotopic fractionation factor, the optimal average value of Pb isotope fractionation factor is also determined. This method is then used for normalizing other Pb isotopic ratios, i.e $^{208}Pb/^{204}Pb$ and $^{208}Pb/^{206}Pb$, but for the Pb isotopic ratios without ^{204}Pb, the Hg interference correction is not needed.

Pb isotope compositions analysed by conventional solution-based method. About 100 mg powders of ferromanganese oxides were sampled at ten different depths from the crust Haxby (Figure S1). The samples were then dissolved in 6M HCl and the Pb cuts were purified by ion chromatography using AG1-X8 resin (Lugmair and Galer, 1992). Pb isotope measurement was carried out on a Thermo Scientific Neptune Plus MC-ICP-MS at GEOMAR, Kiel. Measurements of the Pb isotope compositions were performed as standard

sample bracketing using NBS981 as bracketing standard. Mass bias correction during Pb isotope measurements was done externally using the Tl-doping technique (Belshaw et al., 1998; Süfke et al., 2019) with added NIST997 Tl standard solution. Given that Tl and Pb fractionate slightly differently during ionization, $^{205}Tl/^{203}Tl$ were determined on a session-by-session basis so that NBS981 Pb isotope compositions matched published compositions (Thirlwall, 2002; Baker et al., 2004; Süfke et al., 2019). The external reproducibility was monitored through repeat analyses of secondary standard USGS NOD-A-1. Selected Pb isotope results (2 SD, n = 8) were $^{206}Pb/^{204}Pb$ = 18.965 ± 0.002 and $^{208}Pb/^{204}Pb$ = 2.0544 ± 0.0002. Measured standard Pb isotopic ratios are within the error of published compositions (Baker et al., 2004). Total Pb procedural blanks in were below 50 pg (n=2) and are hence negligible.

Reference material Pb isotope analytical precision and accuracy. As shown in Figure S3, the $^{206}Pb/^{204}Pb$ ratios of standards NIST SRM 610, USGS NOD-A-1 and USGS NOD-P-1 normalized with the linear regression method agree well with literature data (Baker et al., 2004) throughout the analytical sequences. No significant Pb isotopic drift was found during the entire LA-MC-ICPMS measurements (n=230). Two hundred-thirty repeat analyses of these three references over several analytical sessions yielded the following ratios and uncertainties: $^{206}Pb/^{204}Pb$ = 17.053 ± 0.020 and $^{208}Pb/^{206}Pb$ = 2.169 ± 0.001 for NIST SRM 610, $^{206}Pb/^{204}Pb$ = 18.953 ± 0.040 and $^{208}Pb/^{206}Pb$ = 2.054 ± 0.003 for USGS NOD-A-1 and $^{206}Pb/^{204}Pb$ = 18.710 ± 0.124 and $^{208}Pb/^{206}Pb$ = 2.070 ± 0.005 for USGS NOD-P-1 (all uncertainties are quoted as 2 SD). Clearly, the good agreement between the double spike solution data (Baker et al., 2004) and the LA-MC-ICPMS data for three different reference materials show that our measurements were reliable. More outliers were found in NOD references than in the NIST SRM 610 glass due to the inhomogeneous NOD pellet compositions. We found that the matrix had a negligible effect on the Pb isotope analysis by LA-MC-ICPMS under our analytical condition. However, the signal intensity and Hg interference largely controlled the measurement accuracy and precision, and high Pb isotope signal intensities alongside low Hg interferences resulted in highest precision measurements. For instance, although the two NOD references consisted of similar materials, measured Pb isotope data in USGS NOD-A-1 showed smaller standard deviation than in USGS NOD-P-1 because of its higher Pb and lower Hg concentrations in USGS NOD-A-1 than in USGS NOD-P-1. The sample has very similar Pb and Hg concentrations as NIST SRM 610 glass, so we use NIST SRM 610 as the principal standard to evaluate the measurement precision (2SD = ± 0.020 in $^{206}Pb/^{204}Pb$ and 2SD = ± 0.001 in $^{208}Pb/^{206}Pb$), and USGS NOD-A-1/USGS NOD-P-1 as secondary standards.

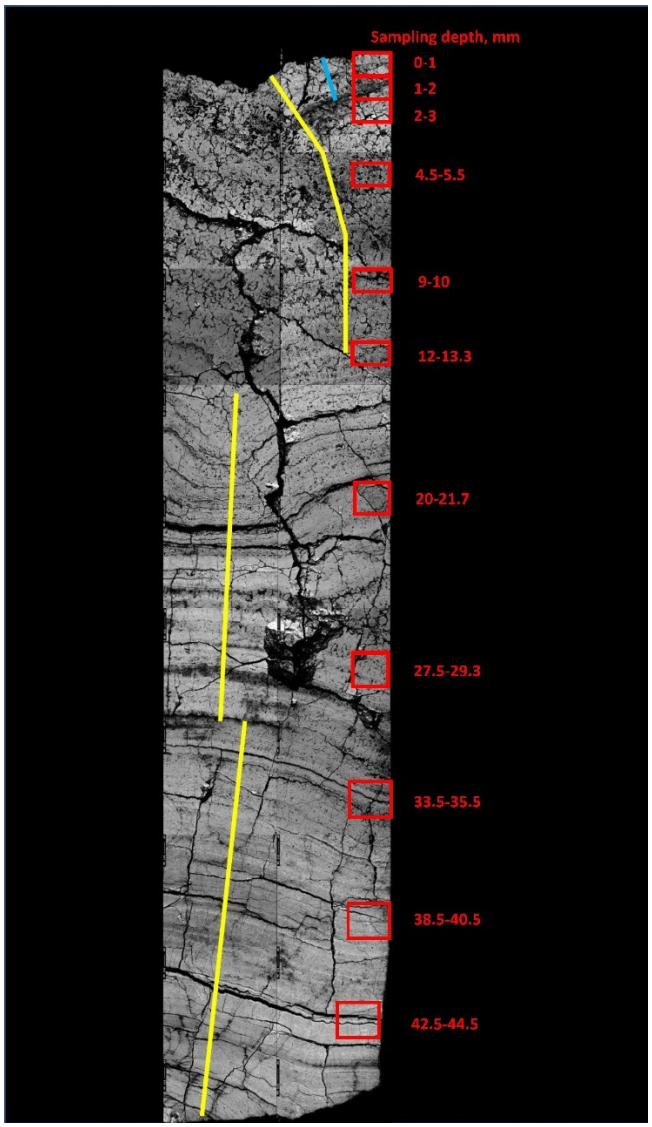

Figure S1. Backscatter Electron (BSE) image of crust Haxby analysed by EMP. The locations of the laser ablation (LA) analyses are indicated by coloured lines (yellow lines indicate 50 microns LA tracks and blue line indicates 15 microns LA track). The red squares indicate the depths of horizons for $^{10}Be/^{9}Be$ dating (0-29.3mm) and conventional Pb isotope analyses (0-44.5 mm).

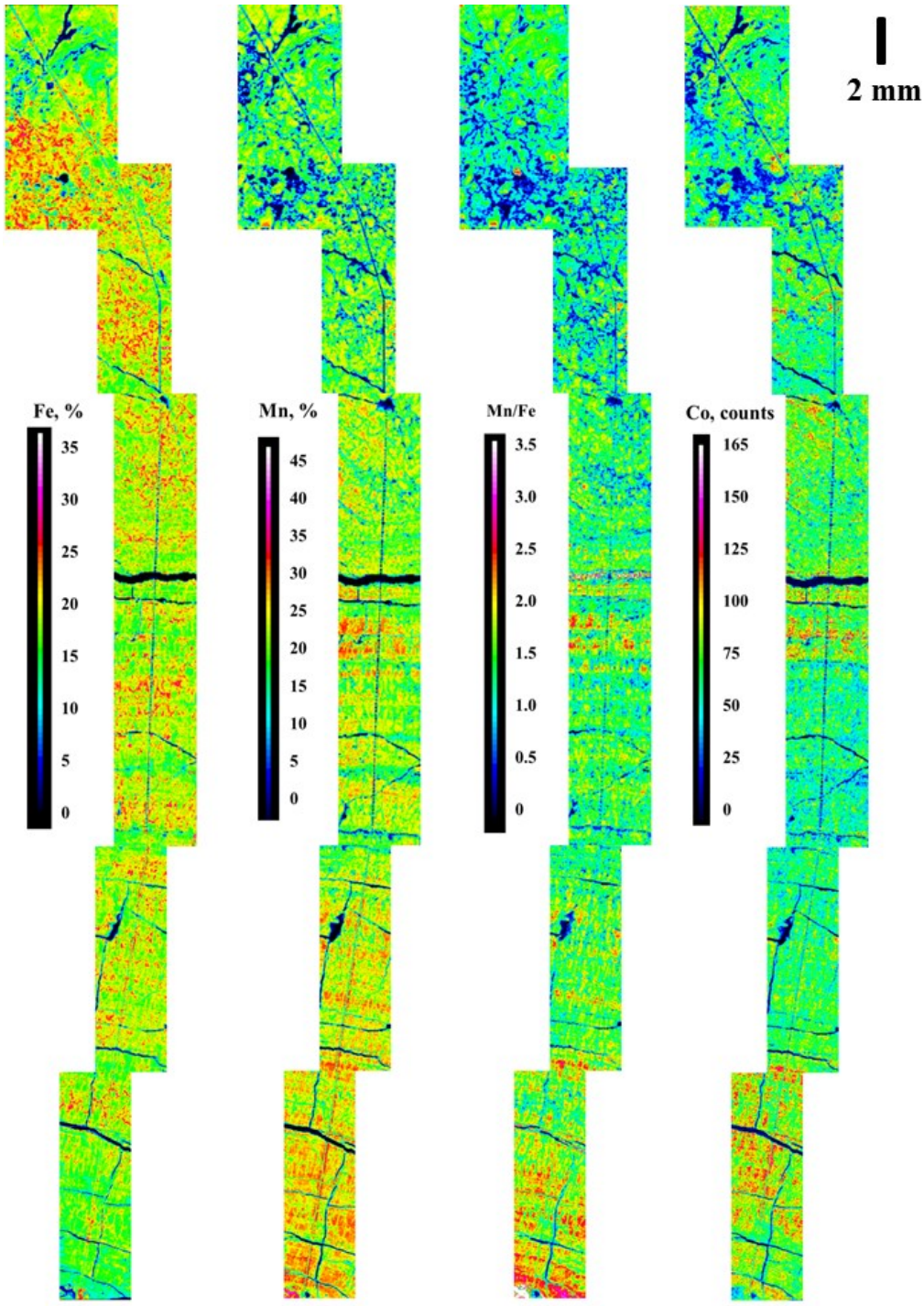

Figure S2. Fe and Mn concentrations, Co intensity (shown as counts per dwell time (20ms)) and Mn/Fe ratio maps of crust Haxby acquired by EMP. The maps were chosen to match the laser ablation tracks.

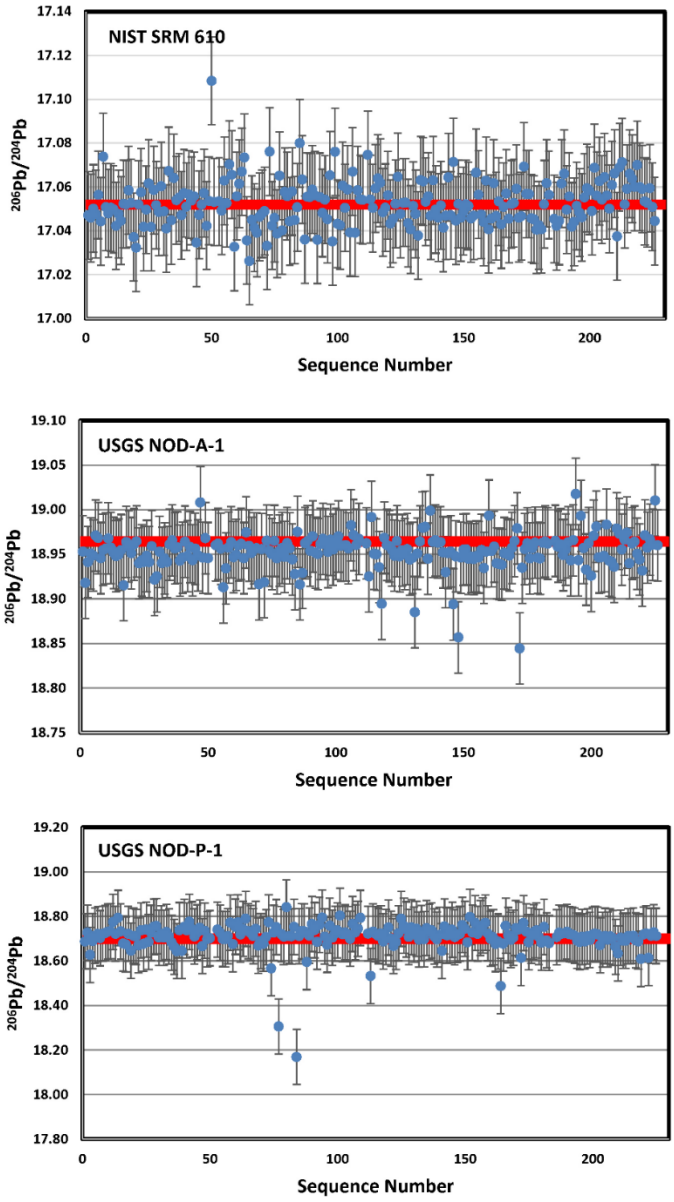

Figure S3. $^{206}Pb/^{204}Pb$ ratios of standard NIST SRM 610, USGS NOD-A-1 and USGS NOD-P-1 normalized by linear regression normalizing method during the LA-MC-ICPMS measurements. The red lines in each figure indicate the literature value (Baker et al., 2004).

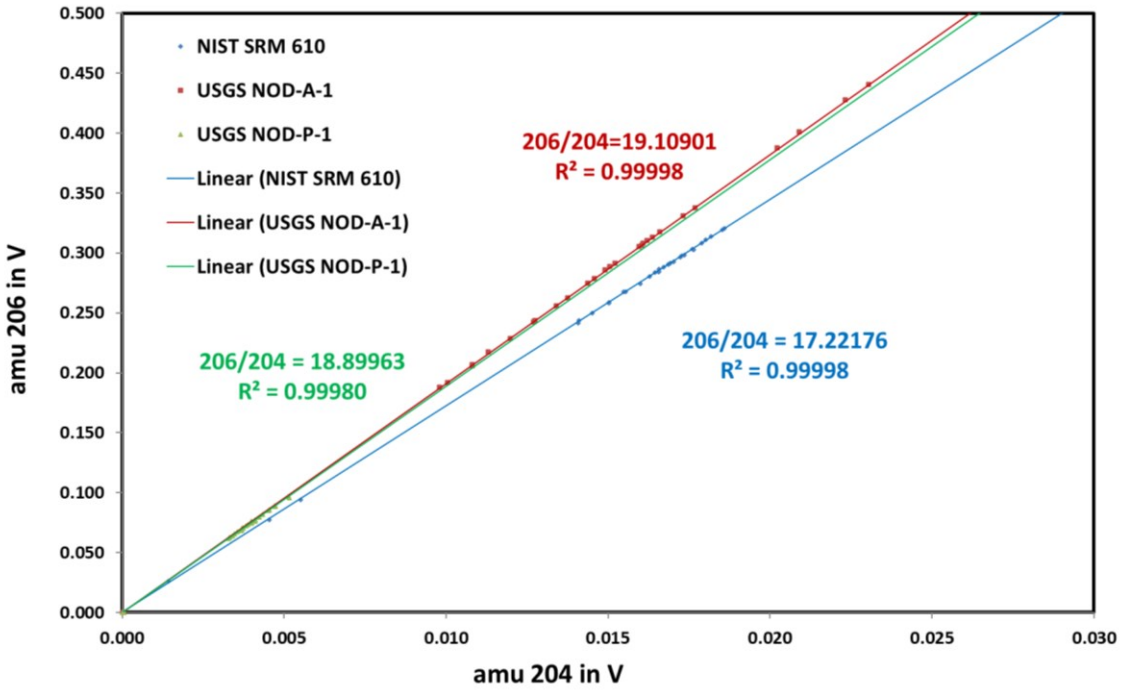

Figure S4. Simultaneous responses of the signals of amu 206 vs. amu 204 for NIST SRM 610, USGS NOD-A-1 and USGS NOD-P-1. The 206/204 show uncorrected $^{206}Pb/(^{204}Pb+^{204}Hg)$ ratios.

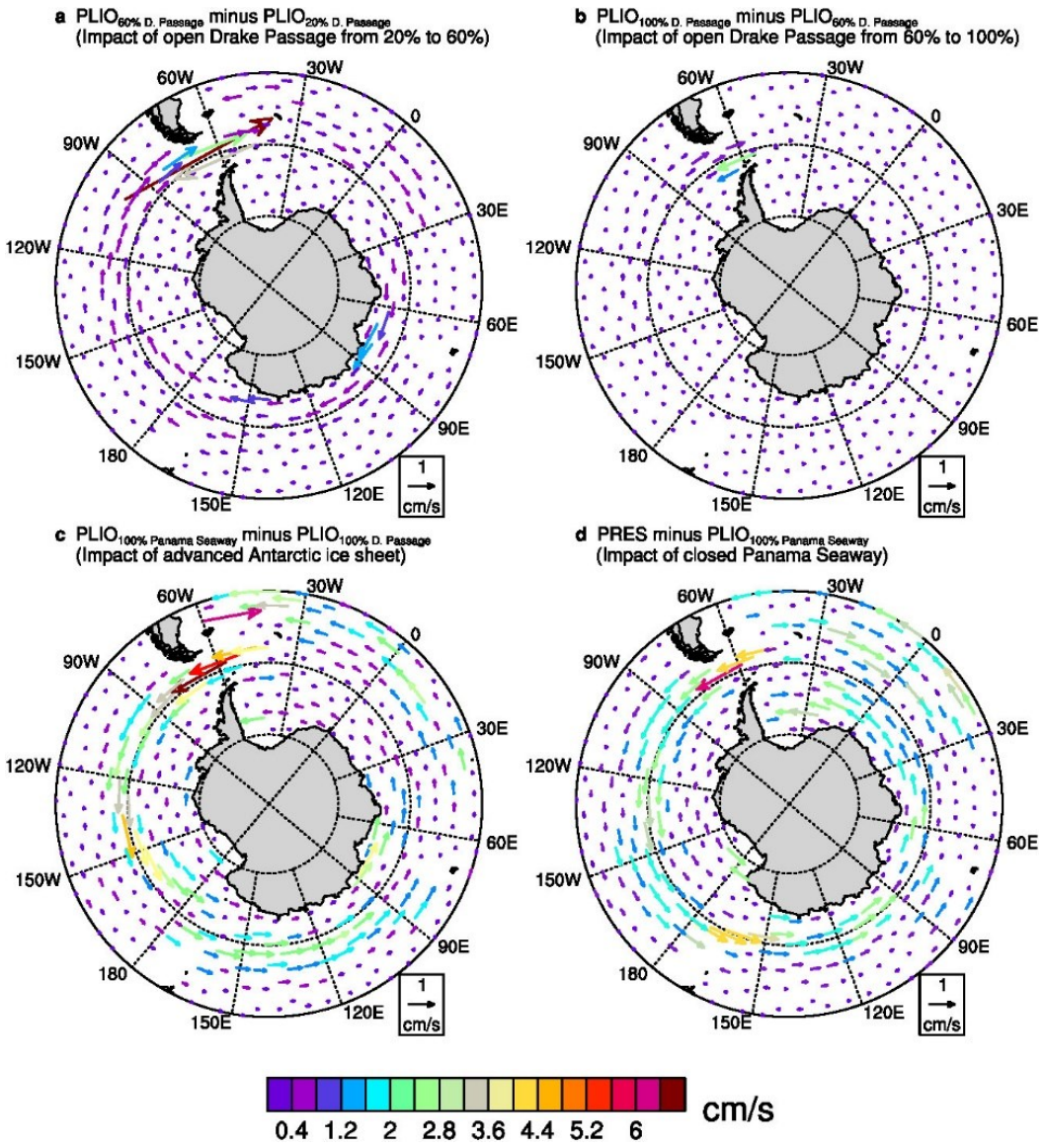

Figure S5. Modelled responses of Southern Ocean circulation at 1830 m water depth. Both the length and colour of the vectors in each map represent the current velocity offsets. The arrow of the vectors indicates the direction of the current velocity offset. a. current changes between a 60% open Drake Passage and a 20% open Drake Passage; b. current changes between a fully open and a 60% open Drake Passage; c. current differences as a result of increased or decreased Antarctic ice volume; d. current differences between a closed and fully opened Panama Seaway.

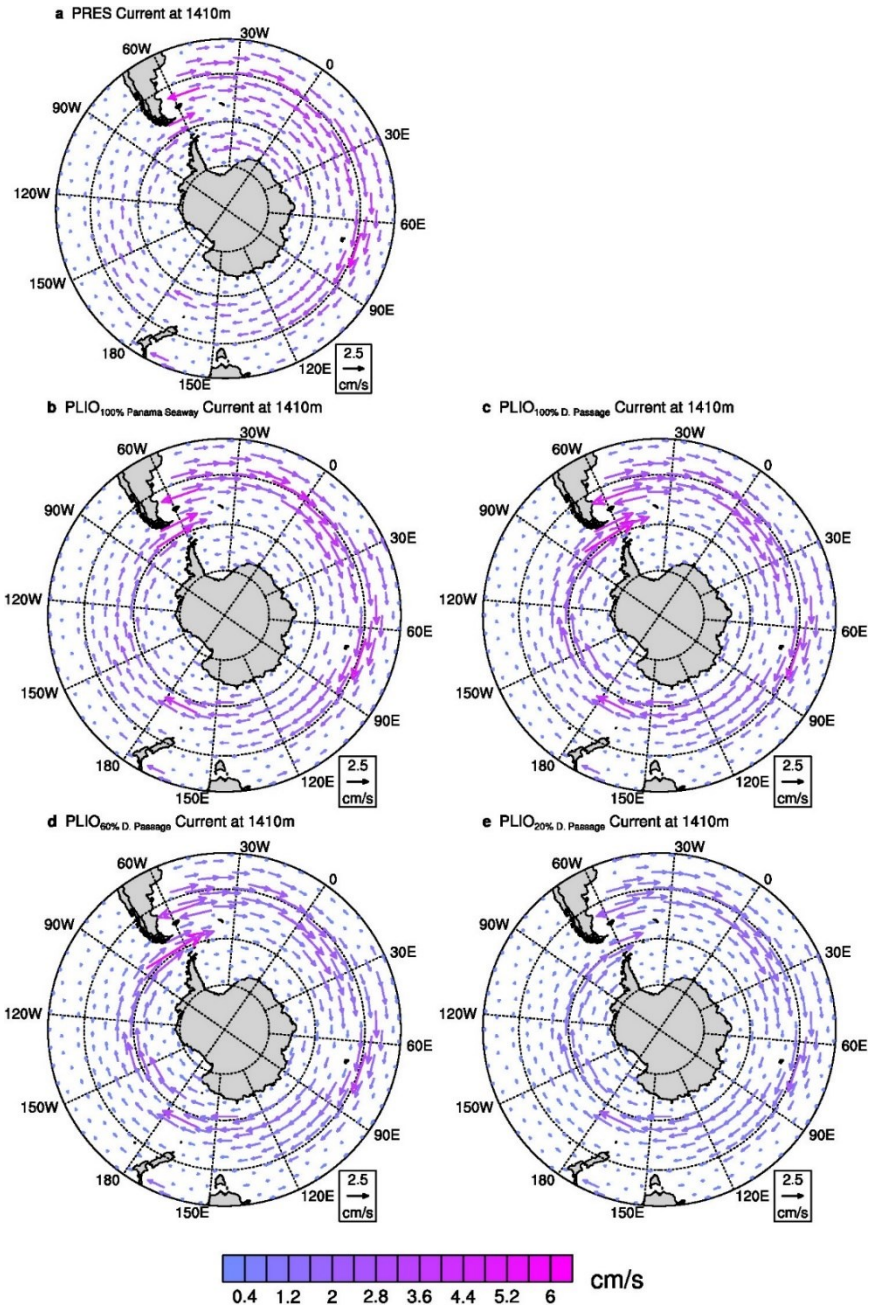

Figure S6. Simulated Southern Ocean circulation current velocity under various tectonic and Antarctic ice volume conditions at 1410 m water depth. a. present-day control run (PRES); b. open of Panama Seaway; c. fully opened Drake Passage with reduced Antarctic ice volume; d. 60% open Drake Passage with reduced Antarctic ice volume; e. 20% open Drake Passage with reduced Antarctic ice volume.

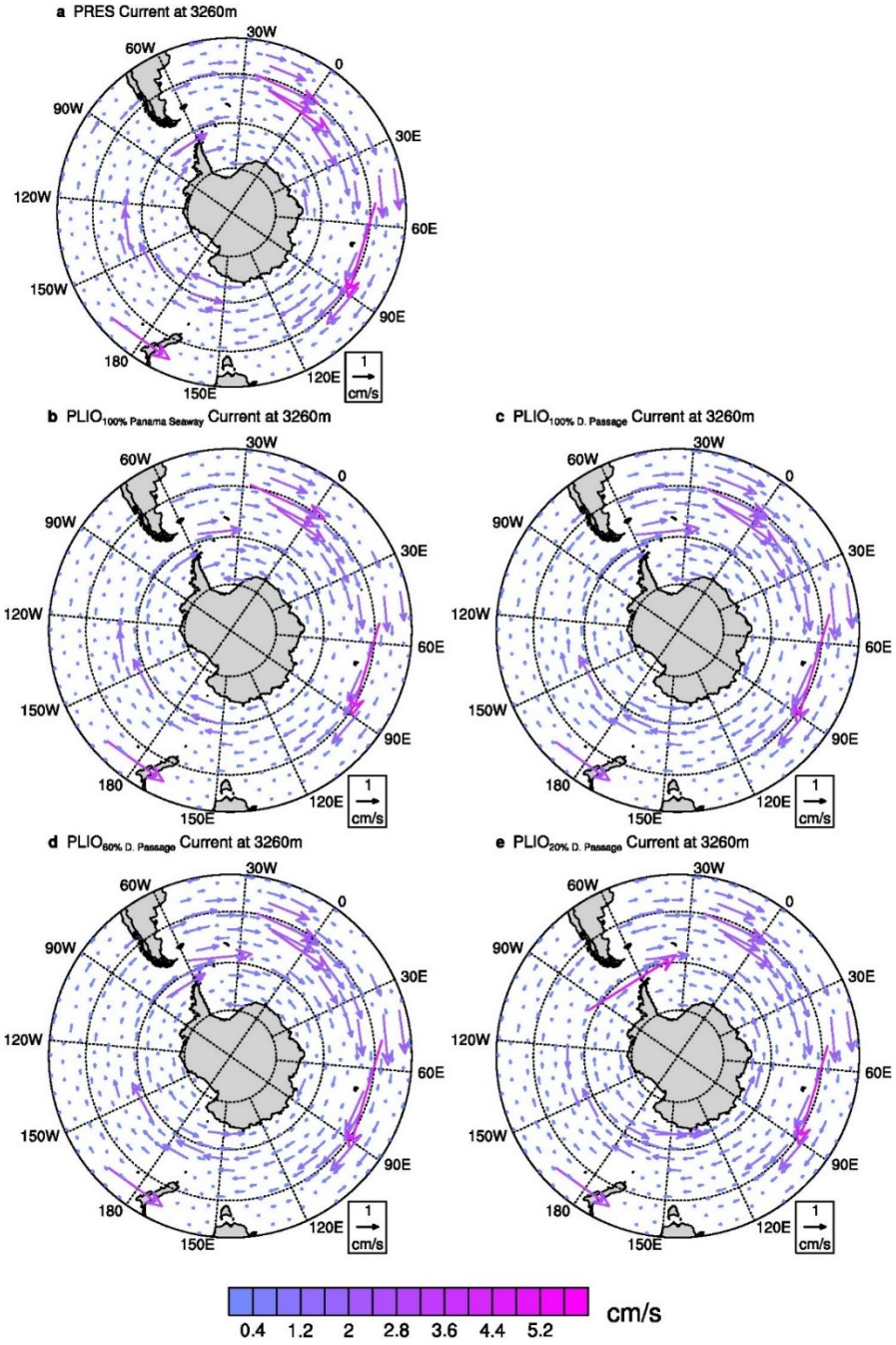

Figure S7. Simulated Southern Ocean circulation current velocity under various tectonic and Antarctic ice volume conditions at 3260 m water depth. a. present-day control run (PRES); b. open of Panama Seaway; c. fully opened Drake Passage with reduced Antarctic ice volume; d. 60% open Drake Passage with reduced Antarctic ice volume; e. 20% open Drake Passage with reduced Antarctic ice volume.

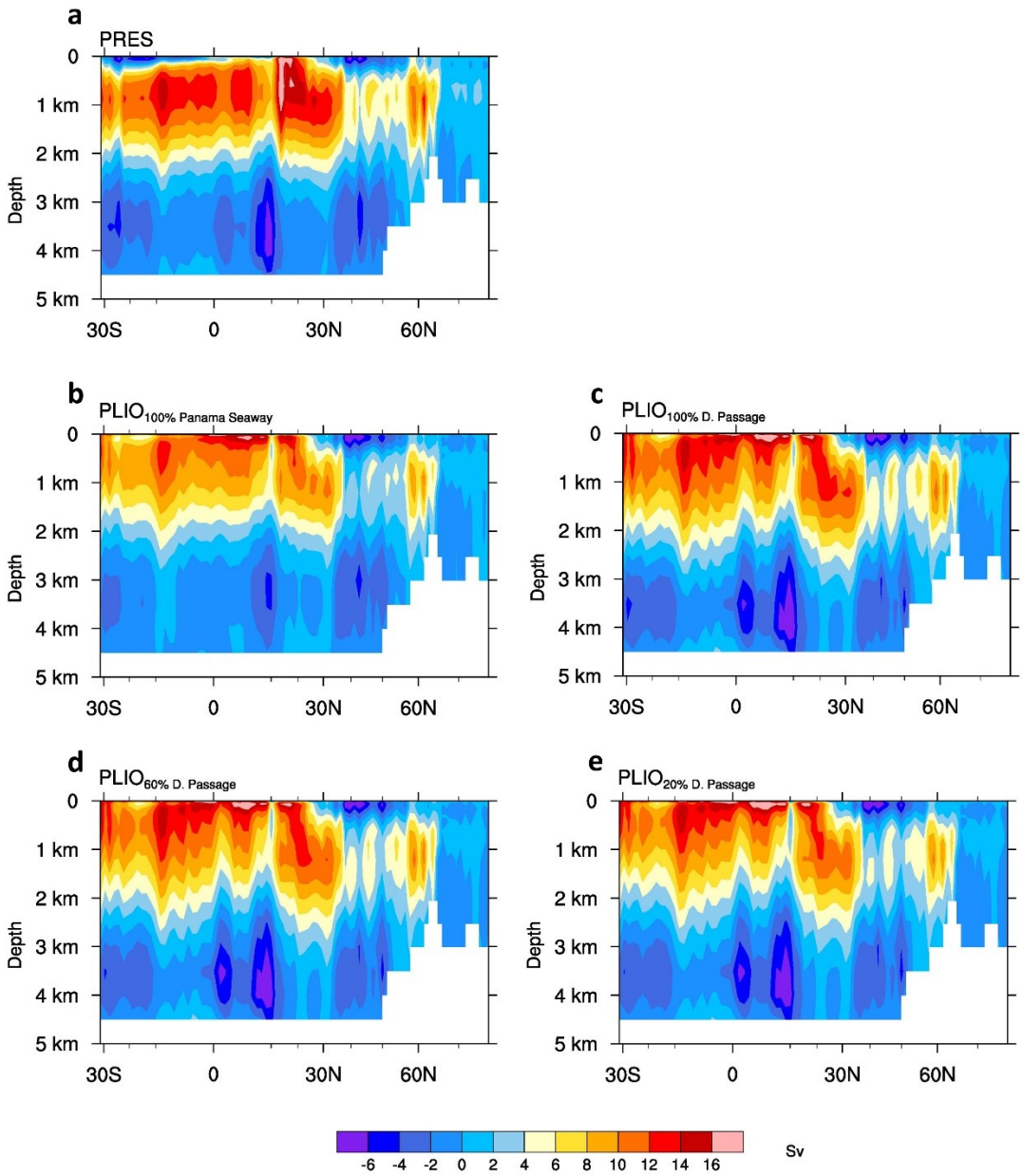

Figure S8. Simulated AMOC under various tectonic and Antarctic ice volume conditions. a. present-day control run (PRES); b. open of Panama Seaway; c. fully opened Drake Passage with reduced Antarctic ice volume; d. 60% open Drake Passage with reduced Antarctic ice volume; e. 20% open Drake Passage with reduced Antarctic ice volume.

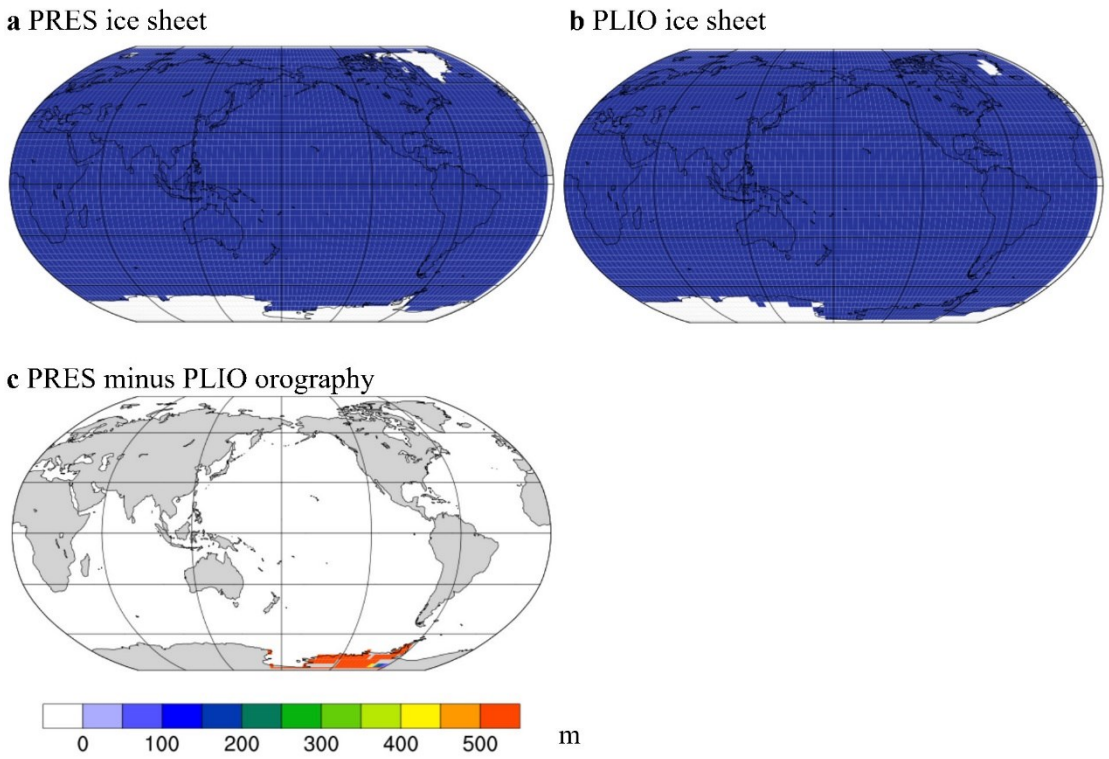

Figure S9. The ice sheet settings in the simulations. The configuration for ice sheet volume is in accordance with the Pliocene Model Intercomparison Project phase 2 protocol (Haywood et al., 2016). a. PRES ice sheet setting; b. PLIO ice sheet configuration. The white colour in a and b indicate the ice sheet extents. c. The difference of ice sheet between PPES and PLIO configurations. The colour bar indicate difference in Antarctic ice sheet thickness.

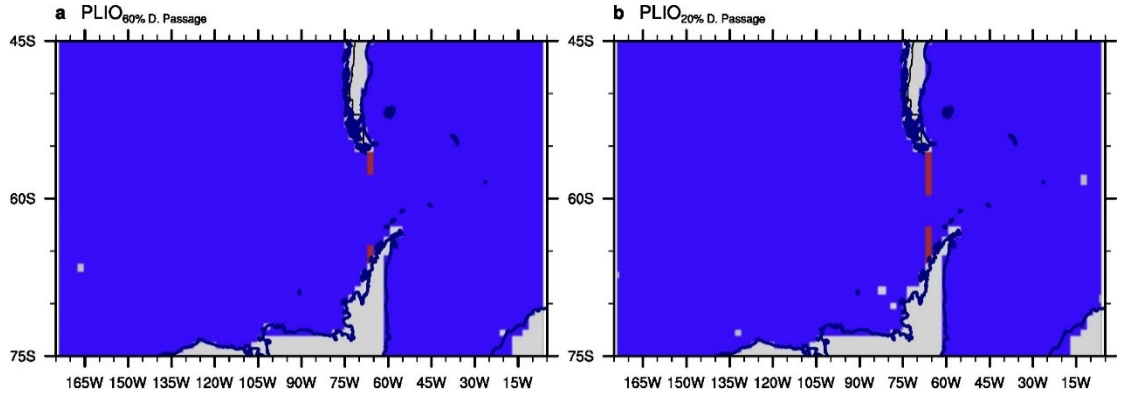

Figure S10. The simulation settings for restricted Drake Passage by adding land grids in Drake Passage. a. 60% relative to the PRES; b. 20% relative to the PRES. The red bars indicate the inserted land grids. The blue and grey shadings indicate the ocean and land regions in the simulation, separately.

Table S1. Be concentrations and $^{10}Be/^{9}Be$-based ages for Fe-Mn crust PS75/247-2 (see Figure S1)

Depth Interval (mm)	^{10}Be ([atoms/g]*10^{-7}), ±1 SE	^{9}Be, ppm	$^{10}Be/^{9}Be$ (*10^{-7}), ± 1 SE	Age (Ma) ±SE
0-1.0	1924.27 ± 38.83	4.517	0.7074 ± 0.038	0.29 ± 0.02
1-2	1739.00 ± 35.12	5.044	0.5725 ± 0.031	0.86 ± 0.05
2-3	1191.46 ± 24.14	4.663	0.4243 ± 0.023	1.44 ± 0.08
4.5-5.5	705.38 ± 14.42	5.825	0.2011 ± 0.011	2.87 ± 0.16
9-10	375.72 ± 14.24	7.746	0.0805 ± 0.005	4.81 ± 0.30
12-13.3	128.73 ± 8.50	5.829	0.0367 ± 0.003	6.17 ± 0.51
20-21.7	26.64 ± 1.70	6.764	0.0065 ± 0.001	9.70 ± 0.79
27.5-29.3	10.72 ± 1.04	7.528	0.0024 ± 0.000	11.75 ± 1.28

Table S2. Instrumental conditions for electron microprobe analysis.

Acceleration voltage	15 kV
Beam current	100 nA
Probe diameter	5 μm
Dwell time	20 ms
Element (channel, crystal)	1) Co (LIFH)
	2) Mn (PETJ)
	3) Fe (LIFH)

Table S3. Calibration of the intensity-concentration conversion using 5x5 pixel maps with the electron microprobe on standards (PbS, Fe_2O_3, VG-2, KAN1, Rhodonite). Concentration (% = percentage weight) is provided as function of the measured intensity in cts = counts

Element	Concentration [%]=f(Intensity [cts])
Fe	C[%] = 0.0140*I[cts]-0.0001
Mn	C[%] = 0.0244*I[cts]-0.0003

Table S4. Incremental growth rates of Fe-Mn crust PS75/247-2. The growth rates were calculated directly by dividing depth interval by age interval. The depths of the Be ages are taken from the median of the depth interval in Figure S1. and the depths for the Co-flux model are taken from the tie points in Figure S3.

Depth Interval (mm)	Growth Rate, mm/Ma	Comments
0-0.5	1.72	Derived from $^{10}Be/^{9}Be$ data
0.5-1.5	1.75	Derived from $^{10}Be/^{9}Be$ data
1.5-2.5	1.72	Derived from $^{10}Be/^{9}Be$ data
2.5-5	1.75	Derived from $^{10}Be/^{9}Be$ data
5-9.5	2.32	Derived from $^{10}Be/^{9}Be$ data
9.5-12.65	2.32	Derived from $^{10}Be/^{9}Be$ data
12.65-20.85	2.32	Derived from $^{10}Be/^{9}Be$ data
20.85-28.4	3.68	Derived from $^{10}Be/^{9}Be$ data
28.4-35.3	3.60	Derived from Co-flux model
35.3-46.95	2.00	Derived from Co-flux model

Table S5. Collector array

L4	L3	L2	L1	Axial	H1	H2	H3	H4
	202	203	204	205	206	207	208	

Table S6. Instrumental parameters of the LA-MC-ICP-MS.

Laser settings	
Ablation cell gas	0.7 l min^{-1} (He)
Spot size	15-140 µm
Fluence	3 J cm^{-2}
Repetition rate	20 Hz
Scan mode	Line with 1 µm s^{-1} scan speed/Line of spots scan with 10 spots
Neptune settings	
Cool gas	16 l min^{-1} (Ar)
Auxiliary gas	0.9 l min^{-1} (Ar)
Nebulizer gas	0.8 l min^{-1} (Ar)
RF power	1200W
Cones	Jet sampler cone/H skimmer cone

Table S7. Instrumental parameters during LA Pb isotope analyses used for samples.

	50 microns LA	15 microns LA
Laser power density	3 J cm^{-2}	3 J cm^{-2}
Repetition rate	20 Hz	20 Hz
Spot size	50 µm	15 µm
Carrier gas	He	He
Scan mode	LA for a 60 µm line with 1 µm/s moving speed	LA for 10 spots in a line (2 s LA and 4 s gas blank for each spot)

Table S8. Instrumental parameters during LA Pb isotope analyses used for standards.

	NIST SRM 610	USGS NOD-A-1	USGS NOD-P-1
Laser power density	3 J cm^{-2}	3 J cm^{-2}	3 J cm^{-2}
Repetition rate	20 Hz	8 Hz	8 Hz
Spot size	140 µm	120 µm	120 µm
Carrier gas	He	He	He
Scan mode	LA at one spot for 60 seconds	LA for a 300 µm line with 5 µm/s moving speed	LA for a 300 µm line with 5 µm/s moving speed

References

Baker, J., Peate, D., Waight, T., Meyzen, C., 2004. Pb isotopic analysis of standards and samples using a 207Pb–204Pb double spike and thallium to correct for mass bias with a double-focusing MC-ICP-MS. Chem. Geol. 211, 275-303, https://doi.org/https://doi.org/10.1016/j.chemgeo.2004.06.030.

Belshaw, N.S., Freedman, P.A., O'Nions, R.K., Frank, M., Guo, Y., 1998. A new variable dispersion double-focusing plasma mass spectrometer with performance illustrated for Pb isotopes. International Journal of Mass Spectrometry 181, 51-58, https://doi.org/https://doi.org/10.1016/S1387-3806(98)14150-7.

Chmeleff, J., von Blanckenburg, F., Kossert, K., Jakob, D., 2010. Determination of the 10Be half-life by multicollector ICP-MS and liquid scintillation counting. Nuclear Instruments and Methods in Physics Research Section B: Beam Interactions with Materials and Atoms 268, 192-199, https://doi.org/https://doi.org/10.1016/j.nimb.2009.09.012.

Christl, M., Vockenhuber, C., Kubik, P.W., Wacker, L., Lachner, J., Alfimov, V., Synal, H.A., 2013. The ETH Zurich AMS facilities: Performance parameters and reference materials. Nuclear Instruments and Methods in Physics Research Section B: Beam Interactions with Materials and Atoms 294, 29-38, https://doi.org/https://doi.org/10.1016/j.nimb.2012.03.004.

Fietzke, J., Frische, M., 2016. Experimental evaluation of elemental behavior during LA-ICP-MS: influences of plasma conditions and limits of plasma robustness. J. Anal. At. Spectrom. 31, 234-244, https://doi.org/10.1039/C5JA00253B.

Fietzke, J., Liebetrau, V., Günther, D., Gürs, K., Hametner, K., Zumholz, K., Hansteen, T.H., Eisenhauer, A., 2008. An alternative data acquisition and evaluation strategy for improved isotope ratio precision using LA-MC-ICP-MS applied to stable and radiogenic strontium isotopes in carbonates. J. Anal. At. Spectrom. 23, 955-961, https://doi.org/10.1039/B717706B.

Frank, M., Eckhardt, J.-D., Eisenhauer, A., Kubik, P.W., Dittrich-Hannen, B., Segl, M., Mangini, A., 1994. Beryllium 10, thorium 230, and protactinium 231 in Galapagos microplate sediments: Implications of hydrothermal activity and paleoproductivity changes during the last 100,000 years. Paleoceanography 9, 559-578, https://doi.org/10.1029/94pa01132.

Frank, M., O'Nions, R.K., Hein, J.R., Banakar, V.K., 1999. 60 Myr records of major elements and Pb–Nd isotopes from hydrogenous ferromanganese crusts: reconstruction of seawater paleochemistry. Geochim. Cosmochim. Acta 63, 1689-1708, https://doi.org/https://doi.org/10.1016/S0016-7037(99)00079-4.

Garbe-Schönberg, C.-D., 1993. SIMULTANEOUS DETERMINATION OF THIRTY-SEVEN TRACE ELEMENTS IN TWENTY-EIGHT INTERNATIONAL ROCK STANDARDS BY ICP-MS. Geostandards Newsletter 17, 81-97, https://doi.org/10.1111/j.1751-908X.1993.tb00122.x.

Haywood, A.M., Dowsett, H.J., Dolan, A.M., Rowley, D., Abe-Ouchi, A., Otto-Bliesner, B., Chandler, M.A., Hunter, S.J., Lunt, D.J., Pound, M., Salzmann, U., 2016. The Pliocene Model Intercomparison Project (PlioMIP) Phase 2: scientific objectives and experimental design. Clim. Past 12, 663-675, https://doi.org/10.5194/cp-12-663-

2016.
Henken-Mellies, W.U., Beer, J., Heller, F., Hsü, K.J., Shen, C., Bonani, G., Hofmann, H.J., Suter, M., Wölfli, W., 1990. 10Be and9Be in South Atlantic DSDP Site 519: Relation to geomagnetic reversals and to sediment composition. Earth Planet. Sci. Lett. 98, 267-276, https://doi.org/https://doi.org/10.1016/0012-821X(90)90029-W.
Lugmair, G.W., Galer, S.J.G., 1992. Age and isotopic relationships among the angrites Lewis Cliff 86010 and Angra dos Reis. Geochim. Cosmochim. Acta 56, 1673-1694, https://doi.org/https://doi.org/10.1016/0016-7037(92)90234-A.
Manheim, F.T., 1986. Marine Cobalt Resources. Science 232, 600-608, https://doi.org/10.1126/science.232.4750.600.
Nishiizumi, K., Imamura, M., Caffee, M.W., Southon, J.R., Finkel, R.C., McAninch, J., 2007. Absolute calibration of 10Be AMS standards. Nuclear Instruments and Methods in Physics Research Section B: Beam Interactions with Materials and Atoms 258, 403-413, https://doi.org/https://doi.org/10.1016/j.nimb.2007.01.297.
Süfke, F., Gutjahr, M., Gilli, A., Anselmetti, F.S., Glur, L., Eisenhauer, A., 2019. Early stage weathering systematics of Pb and Nd isotopes derived from a high-Alpine Holocene lake sediment record. Chem. Geol. 507, 42-53, https://doi.org/https://doi.org/10.1016/j.chemgeo.2018.12.026.
Thirlwall, M.F., 2002. Multicollector ICP-MS analysis of Pb isotopes using a 207Pb-204Pb double spike demonstrates up to 400 ppm/amu systematic errors in Tl-normalization. Chem. Geol. 184, 255-279, https://doi.org/https://doi.org/10.1016/S0009-2541(01)00365-5.